

## Improvement in hot corrosion resistance of dissimilar alloy 825 and AISI 321 CO<sub>2</sub>-laser weldment by HVOF coating in aggressive salt environment at 900°C

*S.M. Muthu*<sup>1)</sup>, *M. Arivarasu*<sup>2)</sup>, *T. Hari Krishna*<sup>1)</sup>, *Supriyo Ganguly*<sup>3)</sup>, *K.V. Phani Prabhakar*<sup>4)</sup>, and *Saurav Mohanty*<sup>5)</sup>

1) School of Mechanical Engineering, VIT, Vellore, Tamil Nadu 632014, India

2) Center for Innovative Manufacture Research, VIT, Vellore, Tamil Nadu 632014, India

3) Welding Engineering and Laser Processing Centre, Cranfield University, Bedford, United Kingdom

4) CLPM, International Advanced Research Centre for Powder Metallurgy & New Materials (ARCI), Hyderabad, India

5) Department of Mechanical Engineering, North Carolina State University, Raleigh, USA

Corresponding author: M. Arivarasu E-mail: arivarasu.m@vit.ac.in; arivarasu.m@gmail.com

(Received: 13 November 2019; revised: 8 February 2020; accepted: 12 February 2020)

### Abstract

This study investigated the hot corrosion performance of a dissimilar weldment of Ni-based superalloy and stainless steel joined by CO<sub>2</sub> laser welding and improved by high-velocity oxy-fuel (HVOF) coating in a Na<sub>2</sub>SO<sub>4</sub>–60wt%V<sub>2</sub>O<sub>5</sub> atmosphere at 900°C. A dissimilar butt joint of AISI 321 and alloy 825 was fabricated by CO<sub>2</sub> laser welding with low heat input after obtaining the optimum welding parameters by bead-on-plate trials. The metallurgical and mechanical properties of the laser weldment were evaluated. The tensile test results indicated the occurrence of fracture in the base metal AISI 321 side. The HVOF process was employed to coat Ni–20wt%Cr on the weldment. To evaluate the surface morphology of the corrosion products formed on the uncoated and HVOF-coated weldments, scanning electron microscopy (SEM) analysis was performed. Energy-dispersive spectroscopy (EDS) was used to determine the different elements present on the surface scales. The existence of oxide phases on the weldments was determined by X-ray diffraction (XRD). The cross sections of the weldments were characterized by SEM with EDS line mapping analysis. The results indicated that the HVOF-coated weldment exhibited superior hot corrosion resistance due to the development of Cr<sub>2</sub>O<sub>3</sub> and NiCr<sub>2</sub>O<sub>4</sub> protective oxide scales.

**Keywords:** nickel-based superalloy; dissimilar welding; weldment corrosion; high-velocity oxy-fuel coating; corrosion kinetics

## 1. Introduction

Superalloys are classified into nickel-, cobalt-, and iron-based alloys. Because of their high-temperature properties, these kinds of materials are mostly preferred for high-temperature applications; thus, they are used in power plants, gas turbines, petrochemical plants, automobiles, aircraft, and waste heat incinerators. In addition, these materials have tremendous mechanical properties such as good yield and tensile behavior, creep strength, corrosion resistance, and erosion at elevated temperatures [1–3]. Nickel-based superalloy 825 is a Ti-stabilized nickel–iron–chromium-based alloy that is mostly used for high-temperature applications; it is used in chemical and petrochemical processing, oil and gas recovery, nuclear fuel processing, and as materials in boilers and superheaters of waste heat incineration system. It has been developed for excellent resistance to corrosion and oxidation and also resistance to stress corrosion cracking. The other elements such as Ni, Mo, and Cu provide resistance in sulfuric and phosphoric acid environments [4–5]. Austenitic stainless steel contains high Cr and Ni contents with added alloying elements such as Mo, Ti, and Nb. The addition of Ti and Nb contents to stainless steel prevents the formation of intermetallic phases and Cr-rich carbides at grain boundaries. The AISI 321 steel is widely used in nuclear power stations, structural components, boilers, superheaters, and chemical reactors [6–8].

During the welding process of dissimilar metals, problems such as solidification cracking, hot cracking, and dilution of weld metals frequently occur due to the difference in composition and thermal expansion between the metals, which change the solidification range. The mechanical properties of stainless steel such as creep, proof, and rupture strengths have been improved by the addition of high Mo, Nb, and Ni contents. Arivarasu *et al.* [9] studied similar laser joints on nickel-based alloy 825 with low heat input and achieved a defect-free weld. The authors studied the metallurgical and mechanical characterization of the weldment. The intermetallic compounds of TiN and Al<sub>4</sub>C<sub>3</sub> observed at the weld interface and weld zone are beneficial for the mechanical strength and hardness of the weldment. Mohanty *et al.* [10] made a similar joining of stainless steel 316 via CO<sub>2</sub> laser welding with a low heat input of 120 J·mm<sup>-1</sup>. Laser welding at low heat input is necessary to realize a small heat-affected zone.

Superalloys are known to have excellent mechanical properties at elevated temperatures. Hot corrosion, which is a surface phenomenon, is detrimental to the service life of a superalloy component, and it can be substantially improved by thermal spray coating [11]. Components in

boilers, superheaters, waste heat incinerators, and gas turbine environments are attacked by corrosion due to the deposition of salts. Most of these failures arise in the hot section of the components, which leads to a reduction in the components life. Many researchers have conducted various tests such as burner-rig test (low-velocity and pressurized burner-rig test), Dean test, electrochemical processes (here, the salt acts as an electrolyte), and crucible and furnace test to determine the hot corrosion behavior of materials. Various salt deposition techniques have been used to apply salts on the specimen, including salt spray, dipping, and hair brushing method. Thermal spray coatings play an essential role in the reduction of corrosion rate at high temperatures; they also enhance the oxidation and corrosion resistances of metals and alloys [11–12]. Various thermal spray coating methods are used to apply protective coatings, such as arc spray coating, flame plasma spray coating, high-velocity oxy-fuel (HVOF), detonation gun, and cold spray coating. The HVOF coating has more advantages over other thermal spray coating technologies, as it results in lower porosity, good adhesion strength, higher hardness, lower decarburization, and high density. Many researchers have reported that HVOF coating exhibits higher corrosion and erosion resistances compared with plasma spraying technologies due to low porosity and higher hardness [13–14]. Sidhu *et al.* [15] reported that HVOF coating has less porosity and better bond strength than most of the other conventional coating techniques. Muthu *et al.* [16] compared the hot corrosion properties of bare and Ni–20wt%Cr-coated superalloy 825 in a molten salt environment. The author reported that the coated specimen exhibited excellent corrosion resistance, while the bare specimen featured a high corrosion rate and spallation. Sidhu *et al.* [17] investigated the hot corrosion behavior of bare HVOF-sprayed Cr<sub>3</sub>C<sub>2</sub>–25wt%NiCr and Ni–20wt%Cr coating on Superni 600 in a molten salt environment of Na<sub>2</sub>SO<sub>4</sub>–60wt%V<sub>2</sub>O<sub>5</sub>. The authors reported that the coating employed by the Ni–20wt%Cr showed less weight gain and also provided superior corrosion resistance than the Cr<sub>3</sub>C<sub>2</sub>–25wt%NiCr coating. This may be attributed to the formation of NiO, Cr<sub>2</sub>O<sub>3</sub>, and spinel NiCr<sub>2</sub>O<sub>4</sub> oxide scales, which acted as a diffusion barrier. Severe oxide scale spallation and corrosion attack were found in the uncoated specimen. Singh *et al.* [18] coated Ni–20wt%Cr on the Ni-based superalloy Nimonic-75 using a cold spray process. The authors studied the hot corrosion behavior of the bare and coated specimens in an actual medical waste heat incineration environment. A high corrosion rate was observed in the uncoated specimen, and the specimen was also subjected to oxy-chlorination in a chlorine environment. The presence of protective chromium-rich scales in the coated specimen enhanced the corrosion resistance. Muthu and Arivarasu [19] deposited Ni–20wt%Cr and Cr<sub>3</sub>C<sub>2</sub>–25wt%NiCr

coating on the Fe-based alloy A-286 using the HVOF process. Hot corrosion study was performed on the bare and coated specimens in an 87.5wt%Na<sub>2</sub>SO<sub>4</sub>–7.5wt%NaVO<sub>3</sub>–5wt%NaCl environment at 700°C. The authors concluded that coating showed a superior corrosion resistance and less corrosion attack, due to the development of oxides of Ni, Cr, and spinel.

In the present work, the dissimilar welding of Ni-based superalloy 825 and AISI 321 austenitic stainless steel was carried out by the CO<sub>2</sub> laser welding process. Such dissimilar welding is required in joining superheater materials in waste heat incineration applications. The joints are attacked by corrosion due to salt deposition from the environment. Thus, they require a protective coating for protection. The hot corrosion properties of the uncoated and coated weldments were investigated in an aggressive Na<sub>2</sub>SO<sub>4</sub>–60wt%V<sub>2</sub>O<sub>5</sub> environment. The thermogravimetric technique was used to determine the corrosion rate. Scanning electron microscopy (SEM) and X-ray diffraction (XRD) methods were used to characterize the surface microstructure and phases of the corrosion products formed on the weldments. The cross sections of the weldments were analyzed to determine the oxide scale thickness and corrosion attack using SEM and energy-dispersive X-ray spectroscopy (EDS) line mapping techniques.

## 2. Experimental

### 2.1. Materials

To conduct the experiment, Ni-based superalloy 825 and austenitic stainless steel AISI 321 were cut into identical sizes (150 mm × 50 mm × 5 mm) using a wire-cut electrical discharge machine (EDM). The as-received alloy 825 was solution-treated at 940°C for 1 h, followed by water quenching. The chemical composition of the as-received samples was obtained by dry spectroscopy and is reported in Table 1.

Table 1. Chemical composition of Alloy 825 and AISI 321 wt%

Material	Ni	Fe	Cr	Mo	Cu	Ti	C	Mn	B
Alloy 825	38.15	29.80	22.27	3.93	2.37	0.71	0.036	0.47	0.002
AISI 321	9.19	69.50	17.35	0.63	0.37	0.28	0.049	1.36	0.001

Bead-on-plate trials were performed to study the penetration profile on the base metal with low heat input. A full-penetration weld of the dissimilar plates (5 mm thickness) of alloy 825 and AISI 321 was obtained using CO<sub>2</sub> laser beam welding after getting the optimum welding conditions

in the bead-on-plate trials (Fig. 1). The autogenous welding was conducted in a completely automated mode to ensure uniform and consistent weld conditions. The optimum parameters that were used to obtain the butt joint are presented in Table 2. The heat input (HI) of the laser welding was  $140 \text{ J} \cdot \text{mm}^{-1}$ , which is calculated by the following formula:

$$HI = \frac{60W}{V}$$

where  $W$  is the laser power in kW, and  $V$  is the travel speed in  $\text{m} \cdot \text{min}^{-1}$ .

Table 2. Process parameters employed during CO<sub>2</sub> laser welding of alloy 825 and AISI 321

Output power / kW	Frequency / Hz	Wavelength / $\mu\text{m}$	Excitation	Beam quality	Power stability / %	Focal length / mm	Beam diameter / $\mu\text{m}$
3.5	5000	10.6	Radio frequency	>0.9	$\pm 2$	300	180

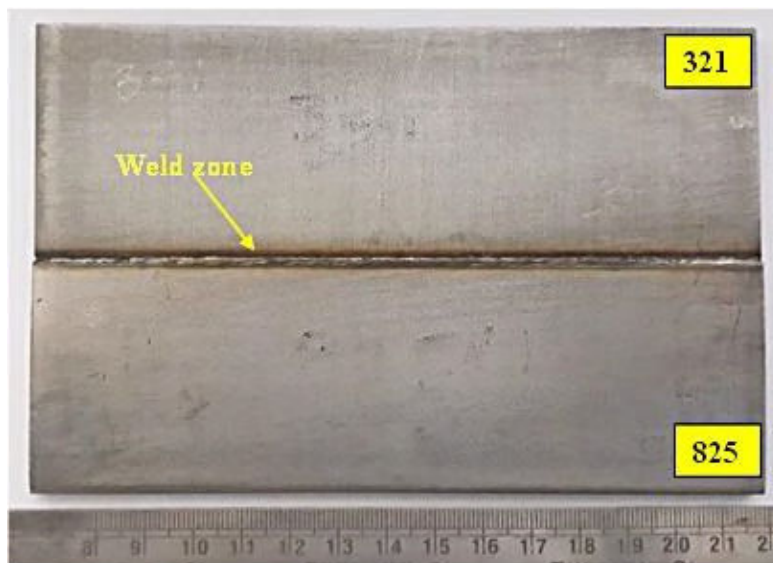


Fig. 1. Photograph of 825–321 dissimilar CO<sub>2</sub> laser weldments.

## 2.2. Characterization of weldment

For microstructure study, the composite region (weld zone with base metal) from the CO<sub>2</sub> laser-welded sample in the transverse direction of the weldment was used. The sample was polished with SiC emery papers of 400, 800, and 1200 grit size, and then polished with alumina slurry on a velvet cloth disk to obtain a mirror-like finish. The weldment was subjected to electrochemical etching using a 10wt% oxalic acid solution with a 6 V DC supply and a current density of 1.6 A·cm<sup>-2</sup> at room temperature. The microstructures of the base metals, weld zone, and weld interface were characterized using optical microscopy.

### 2.3. Evaluation of mechanical properties

The mechanical properties of the 825–321 dissimilar weldment were evaluated using tensile test, impact test, and microhardness test. The tensile test was performed on a cut-out sample (100 mm × 10 mm × 5 mm) from the welded plates as per the ASTM E8/8M standard. Two specimens were tested to understand the variation and validate the tensile properties of the weld. The cross-head velocity parameter for the tensile testing was set at 1 mm·min<sup>-1</sup>. The Charpy impact test was done as per the ASTM E23-12C standard. A 45° V-notch was made over the weldment to perform the Charpy impact test. The Vickers microhardness test was performed across the cross sections of three regions of the sample, with a load of 5 N and dwell time of 10 s. The measurement was carried out with a distance of 0.25 mm.

### 2.4. HVOF coating

For the HVOF coating, a composite region (weld zone with base metal) of 20 mm × 10 mm × 5 mm was extracted from the weldment using a wire-cut EDM. Before coating, the sample was ground with SiC papers and subsequently grit-blasted with alumina particles to ensure the roughness of the specimen. The purpose of grit blasting is to enhance the adhesion strength between the substrate and coating. Using the HVOF process, Ni–20wt%Cr powder was deposited on the weldment. The process parameters employed for the HVOF coating are reported in Table 3.

Table 3. Process parameters employed for the HVOF coating

Oxygen pressure / (N·mm <sup>-2</sup> )	Oxygen flow rate / (L·min <sup>-1</sup> )	Hydrogen pressure / (N·mm <sup>-2</sup> )	Hydrogen flow rate / (L·min <sup>-1</sup> )	Powder feed / (g·min <sup>-1</sup> )	Powder particle size / μm	Spray distance / mm
1.07–1.14	14–16	0.78–0.88	26–30	80–100	64	230

## **2.5. Molten salt corrosion study**

The cyclic hot corrosion experiment was carried out on bare and coated 825–321 dissimilar weldments for 50 cycles under cyclic conditions. Every cycle consisted of 1 h heating at 900°C, followed by 20 min of cooling at room temperature. A layer of Na<sub>2</sub>SO<sub>4</sub>–60wt%V<sub>2</sub>O<sub>5</sub> salt was coated on all sides of the weldments using a hairbrush in the range of 3.0 to 5.0 mg·cm<sup>-2</sup> with a uniform thickness. The salt-coated specimen was then preheated to 250°C for 2 h to remove the moisture content. The weight change of the samples was measured along with the spalled scales at the end of each cycle.

The weight change measurement was used to determine the corrosion rate by the thermogravimetric technique. After the hot corrosion experiments were completed, the weldments were analyzed by SEM/EDS for surface morphology and composition analysis, and XRD was used for phase identification. Moreover, EDS line mapping analysis was done on both bare and coated weldments at cross sections. The oxide scale formation and corrosion attack were found using cross-sectional SEM analysis.

## **3. Results and discussion**

### **3.1. Microstructure analysis**

Delta ferrites were observed along the rolling direction in the austenitic stainless steel (AISI 321) base metal microstructure. From the optical microstructure, alloy 825 showed an austenitic structure. Major heat-affected zones were not observed in the sample because the laser welding was conducted with low heat input, and thus, it was challenging to observe heat-affected zones. Columnar and cellular structures were observed in the fusion zone, as illustrated in Fig. 2.

### **3.2. Microhardness**

Fig. 3 illustrates the microhardness profile of 825–321 dissimilar laser weldments. The hardness dropped comparatively while progressing toward the weld interface from the alloy 825 regions. The average hardness values of the alloy 825, weld zone, and AISI 321 were HV 170.8, HV 177.9, and HV 166.2, respectively. The microhardness profile shows that all the regions presented similar hardness values.

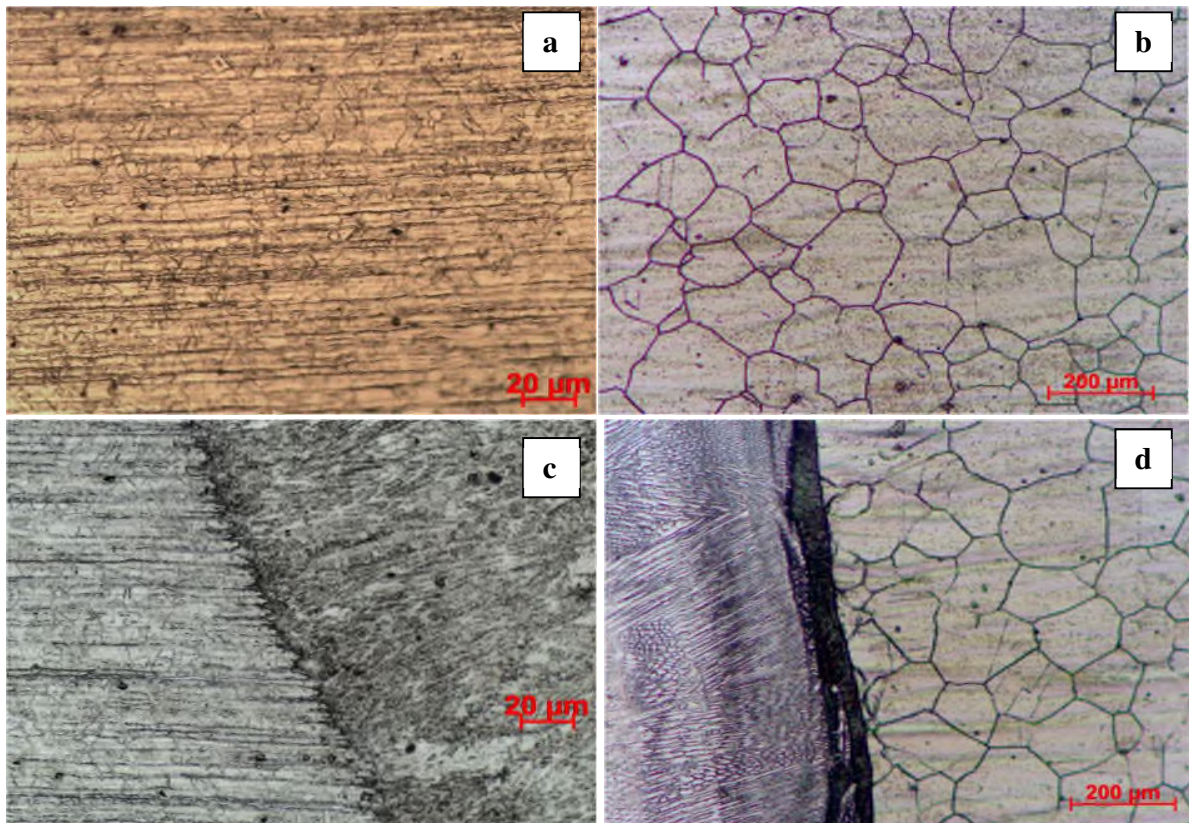


Fig. 2. Optical microstructures of the base metals and interfaces of dissimilar CO<sub>2</sub> laser weldments: (a) base metal AISI 321; (b) alloy 825; (c) 321 weld interface; (d) 825 weld interface.

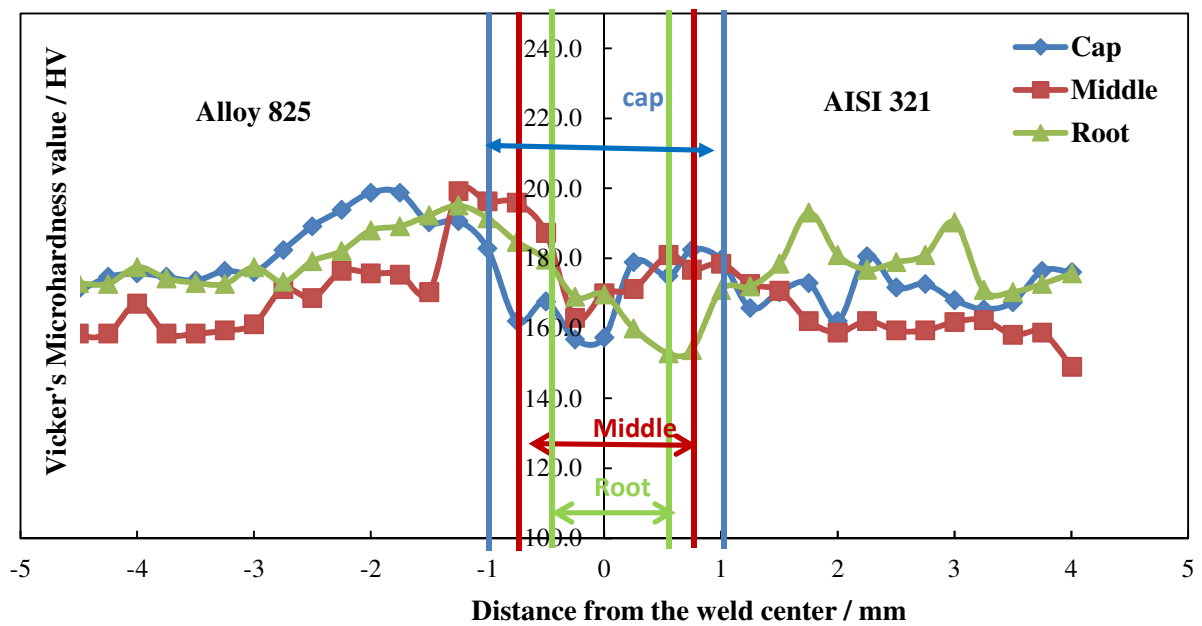


Fig. 3. Microhardness profile of 825-321 dissimilar CO<sub>2</sub> laser weldments.



### 3.3. Tensile test

Transverse tensile tests were performed on the laser-welded dissimilar joint to evaluate the ductility and weld strength. The photograph of the tensile sample before the testing is shown in Fig. 4(a). The average tensile strength of the dissimilar laser weldment was 681.5 MPa. After the tensile test, the mode of fracture was found to occur at the base metal near the weld zone of the alloy 321 region, which is shown in Fig. 4(b). The SEM fractograph (Fig. 4(c)) revealed a ductile fracture mode.

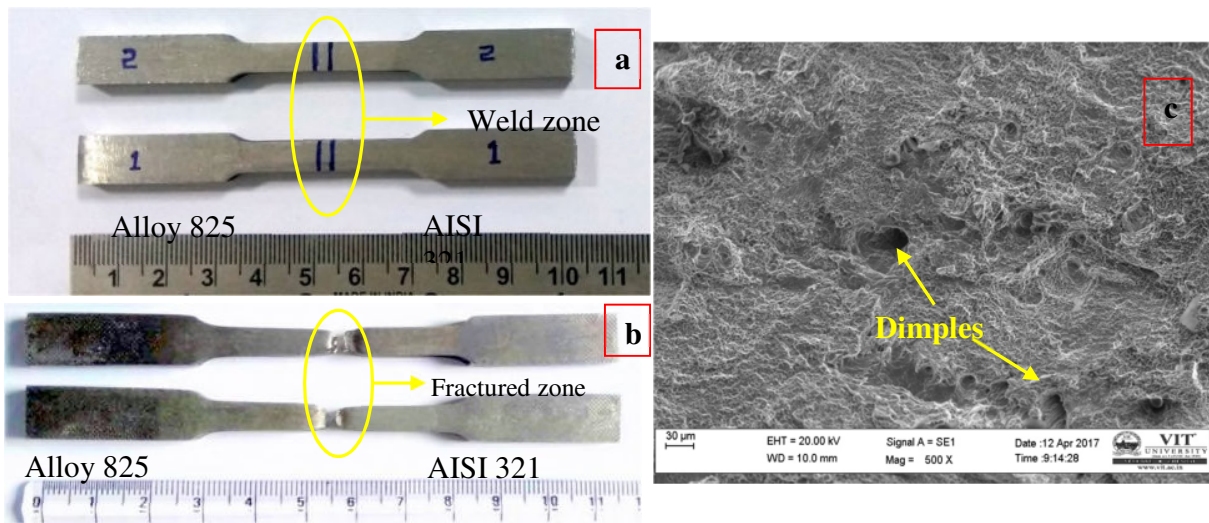
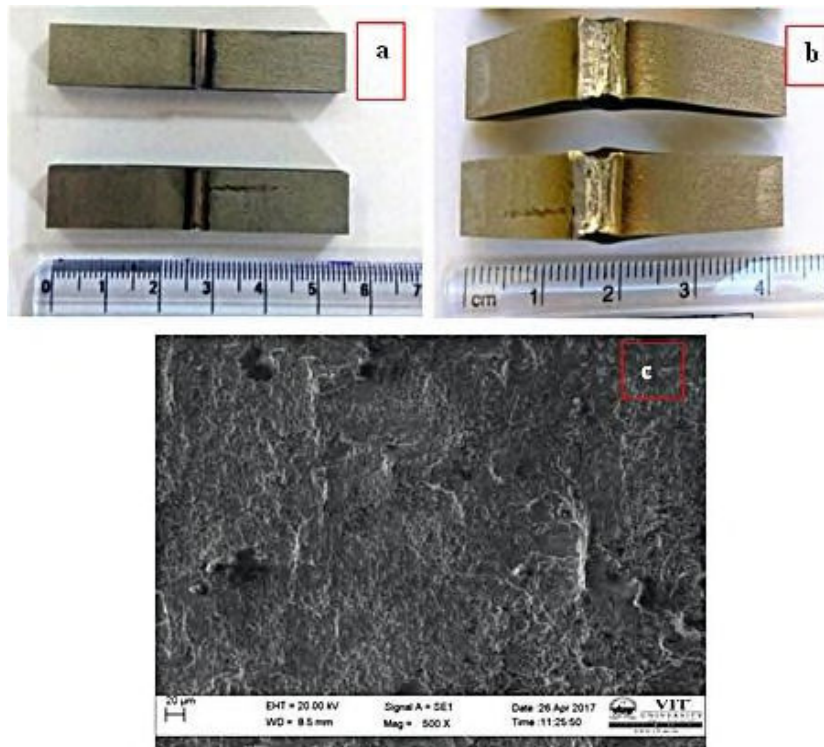


Fig. 4. (a) Laser-welded tensile testing samples; (b) the samples after the tensile test; (c) SEM fractograph of the tensile sample.

### 3.4. Impact test

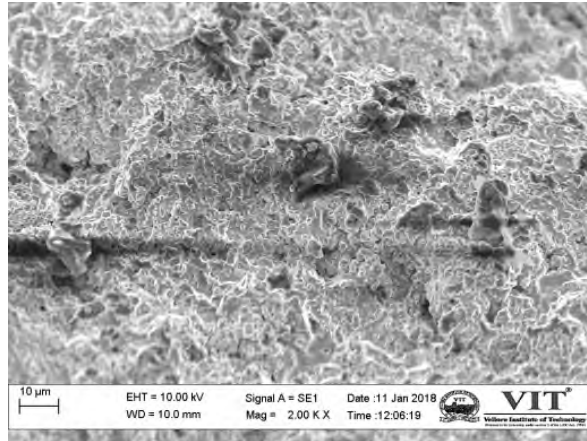
The toughness of the dissimilar weld joint was evaluated using the Charpy V-notch method. The photographs of the impact test specimens are shown in Figs. 5(a) and 5(b). The average toughness value of the weldment was  $72.1 \text{ J}\cdot\text{m}^{-2}$ . After the impact test, the fractured sample was characterized by SEM to evaluate the fracture mode. The SEM fractograph (Fig. 5(c)) reveals that the dissimilar laser joint showed a ductile fracture mode, which was analyzed by studying the microvoids and dimples.



**Fig. 5.** Photographs of (a) laser-welded impact testing sample with V-notch and (b) sample after the impact test; (c) SEM fractograph of the impact sample.

### 3.5. SEM microstructure of the coating

The surface roughness of the HVOF-sprayed Ni-20wt%Cr coating on the weldment was measured using a Mahr surface roughness tester. The centerline average method was used to measure the roughness value of the coating. Measurements were conducted at three different places of the coating surface, and then the average value was taken. The average roughness value of the Ni-20wt%Cr coating was 5.86 µm. The SEM-derived surface morphology of the Ni-20wt%Cr coating deposited by HVOF (Fig. 6) shows the existence of partially and fully melted particles. The coating seemed to be uniform and dense, and exhibited a compact interlocked structure, which are distinct features of the HVOF coating process. Splats boundaries along with some micro-cracks occurred on the coating surface, which may be attributed to the high impact speed of the HVOF coating technique.




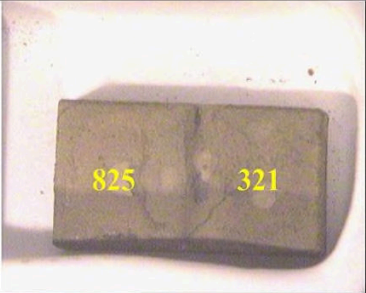
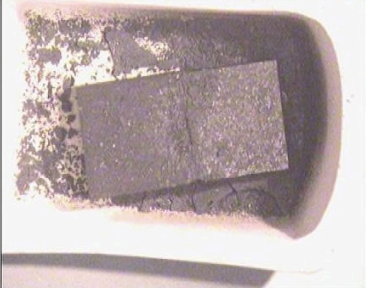
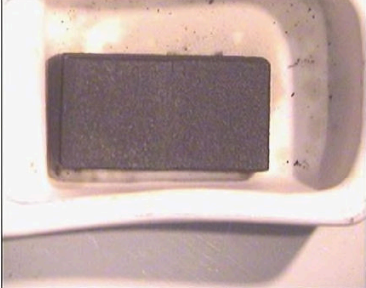
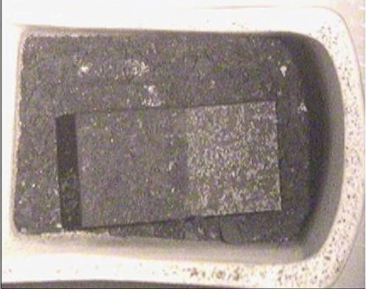
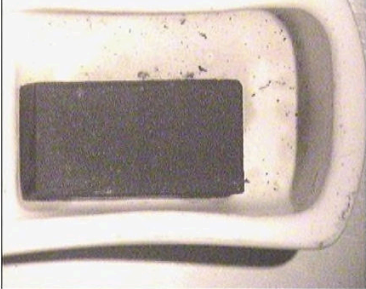
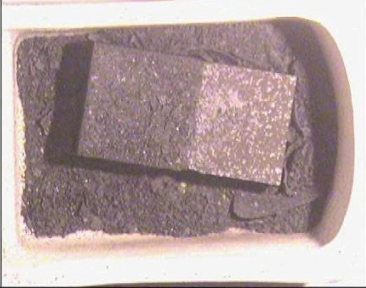
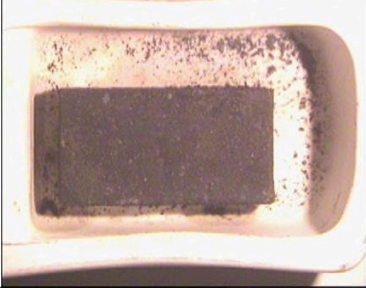
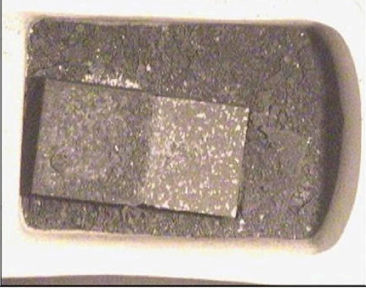
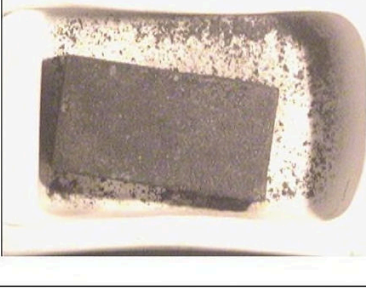
**Fig. 6.** SEM microstructure of the as-sprayed Ni–20wt%Cr coating on the weldment.

### 3.6. Visual inspection

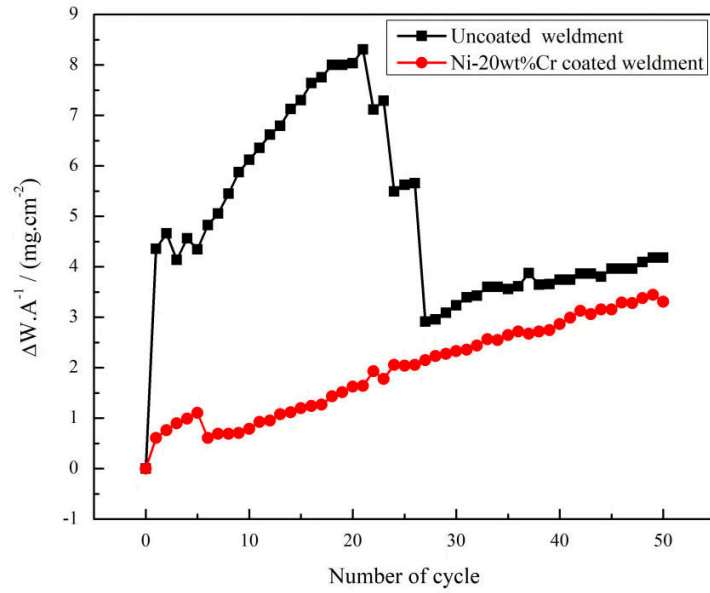
Macro-images of the uncoated and coated weldments during exposure to the salt environment are depicted in Fig. 7. The macro-images show the presence of oxide scales on the surface, spallation, and sputtering. In the uncoated weldment, from the initial stage onward, the scales started to spall on both the weld and base metal regions. This could be attributed to the extensive corrosion at the AISI 321 region and the weld zone caused by the development of the  $\text{Fe}_2\text{O}_3$  scale. The spalling rate of scales increased with an increase in exposure time, as shown in Fig. 7. A minor oxide scale spallation was observed in the coated specimen.

### 3.7. Thermogravimetric analysis

The weight gain plots of the uncoated and coated weldments are depicted in Fig. 8, where  $\Delta W$  is the weight gain, and  $A$  is surface area. The uncoated weldment showed a higher corrosion rate compared with the HVOF-coated weldment. During the initial stage of the hot corrosion study, high weight gain could be found in both specimens, which was due to the development of new oxide scales on weldments [17]. The uncoated weldment exhibited a high weight gain of  $8.307 \text{ mg}\cdot\text{cm}^{-2}$  at the 21<sup>st</sup> cycle, after which the weight started to decrease; this decrease was attributed to the spalling of oxide scales outside the crucible. Thus, calculating the corrosion rate for the uncoated specimens is difficult. A similar result has been reported by Muthu *et al.* [16]. The HVOF coating showed less weight gain ( $3.305 \text{ mg}\cdot\text{cm}^{-2}$ ) and also provided better resistance to corrosion. This indicates that the coating surface was protected due to the presence of NiO and  $\text{Cr}_2\text{O}_3$  oxide scales.

Cycles	Uncoated weldment	HVOF coated weldment
0 <sup>th</sup> Cycle	 A rectangular metal specimen with yellow markings '825' and '321' on its surface, placed in a white ceramic tray.	 A rectangular metal specimen with yellow markings '825' and '321' on its surface, placed in a white ceramic tray.
10 <sup>th</sup> cycle	 The uncoated specimen is heavily corroded, with a dark, porous layer of corrosion products covering most of its surface.	 The HVOF-coated specimen shows a dark, uniform layer of corrosion products, with the underlying metal surface still visible.
25 <sup>th</sup> Cycle	 The uncoated specimen is almost completely covered by a thick, dark, porous layer of corrosion products.	 The HVOF-coated specimen shows a dark, uniform layer of corrosion products, with the underlying metal surface still visible.
40 <sup>th</sup> Cycle	 The uncoated specimen is almost completely covered by a thick, dark, porous layer of corrosion products.	 The HVOF-coated specimen shows a dark, uniform layer of corrosion products, with the underlying metal surface still visible.
50 <sup>th</sup> cycle	 The uncoated specimen is almost completely covered by a thick, dark, porous layer of corrosion products.	 The HVOF-coated specimen shows a dark, uniform layer of corrosion products, with the underlying metal surface still visible.

**Fig. 7.** Macro-images of uncoated and HVOF-coated hot-corroded weldments during exposure to molten salt at 900°C.



**Fig. 8.** Thermogravimetric analyses of uncoated and HVOF-coated weldments after subjection to hot corrosion in  $\text{Na}_2\text{SO}_4\text{-60wt\%V}_2\text{O}_5$  molten salt environment at  $900^\circ\text{C}$ .

Fig. 9 shows that the relationship of  $(\Delta W \cdot A^{-1})^2$  versus the number of cycles for the coated specimen follows the parabolic law, while that for the uncoated weldment follows the parabolic law till the 21<sup>st</sup> cycle, after which it deviates. The corrosion rate of the weldments can be calculated by  $(\Delta W \cdot A^{-1})^2 = K_p \times t$ , where  $K_p$  represents a parabolic constant,  $t$  is exposure time in s. The weight gains and parabolic rate constants ( $K_p$ ) of the coated and uncoated samples are presented in Table 4. The parabolic rate constant ( $K_p$ ) was obtained from the slope of the linear regression fitted line for  $(\Delta W \cdot A^{-1})^2$  versus the number of cycles. The nature of fit depends on the square of the weight gain  $(\Delta W \cdot A^{-1})^2$  for the specimen and is directly related to the weight loss and weight gain pattern of the sample. This suggests that if the material has good hot corrosion resistance, the fit will be a straight line and follow the parabolic rate law.

Table 4. Weight gains and corrosion kinetics of the weldments

Material	$\Delta W \cdot A^{-1} / (\text{mg} \cdot \text{cm}^{-2})$	$K_p / (10^{-10} \text{ g}^2 \cdot \text{cm}^{-4} \cdot \text{s}^{-1})$
Uncoated sample	8.307 (21 <sup>st</sup> cycle)	9.613
HVOF-coated sample	3.305	0.607

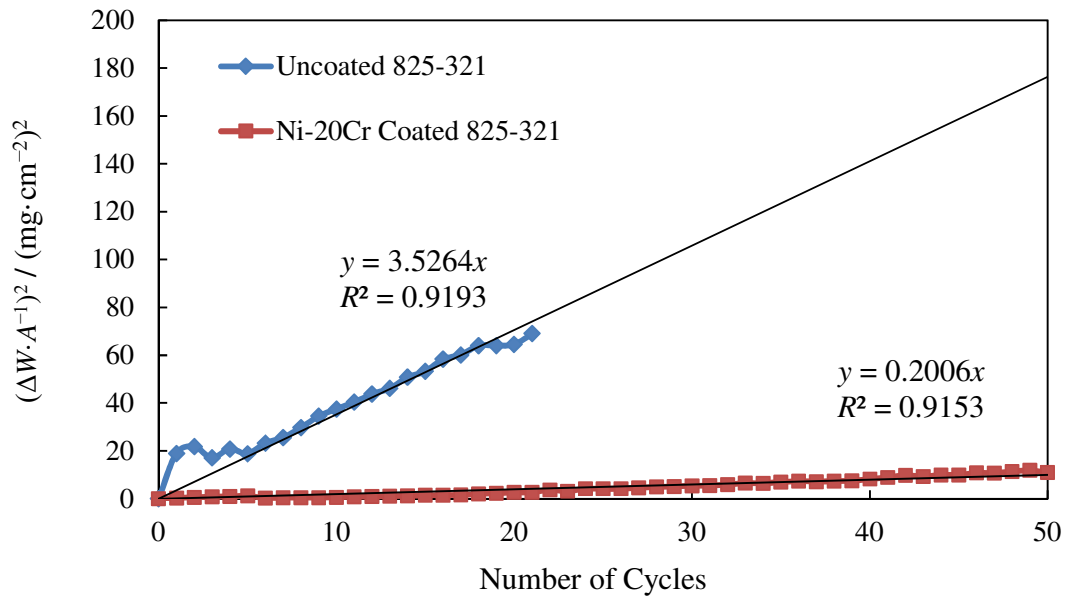


Fig. 9. Plots of  $(\Delta W \cdot A^{-1})^2$  vs. number of cycles for uncoated and HVOF-coated weldments after hot corrosion at 900°C.

### 3.8. SEM/EDS analysis

The SEM microstructures of the hot-corroded uncoated and HVOF-sprayed 825–321 dissimilar laser weldments are described in Figs. 10 and 11, respectively. The SEM morphology of the uncoated weldment (Fig. 10) shows the existence of cracks in the oxide scales and the spalled region. The alloy 825 region featured an uneven surface due to oxide scale spallation, and cracks were also observed. The EDS analysis results reveal the presence of high contents of Fe, O, and Ni, with a moderate amount of Cr. This suggests the existence of NiO, Cr<sub>2</sub>O<sub>3</sub>, and Fe<sub>2</sub>O<sub>3</sub> scales. In the weld region, a particle-shaped microstructure, as well as a spalled region, was observed. The EDS analysis of the particle-shaped structure shows the formation of Fe<sub>2</sub>O<sub>3</sub>, Cr<sub>2</sub>O<sub>3</sub>, and NiO scales. The AISI 321 region mainly consisted of O and Fe, with a small amount of Ti, Ni, and Cr. Corrosive elements Na, S, and V were found in all the regions of the weldment. Considering the Ni–20wt%Cr-coated weldment, the SEM microstructure (Fig. 11) (weld and base metal region) exhibited a rough surface, and cracks were observed on the surfaces. Higher amounts of oxygen, nickel, and chromium with minor amounts of Fe, Na, V, and S were observed in the oxide scales of the coated weldment.

Moreover, alloying elements were present in the uncoated and HVOF-coated weldments after hot corrosion, and they are listed in Tables 5 and 6.

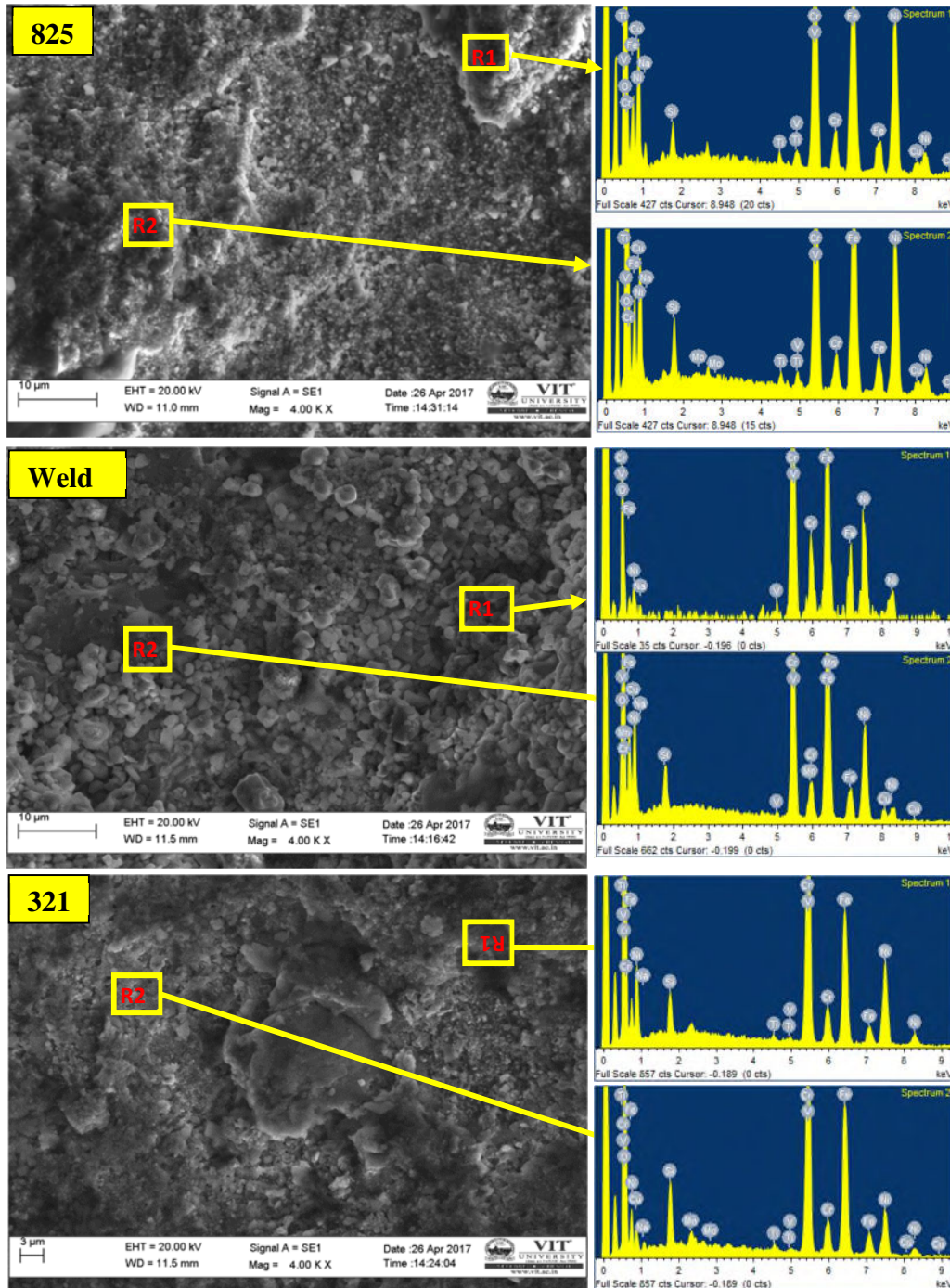


Fig. 10. SEM/EDS analysis of the uncoated 825–321 CO<sub>2</sub> laser weldments after hot corrosion in Na<sub>2</sub>SO<sub>4</sub>–60wt%V<sub>2</sub>O<sub>5</sub> environment at 900°C for 50 cycles (R1 and R2 correspond to Region 1 and Region 2, respectively).

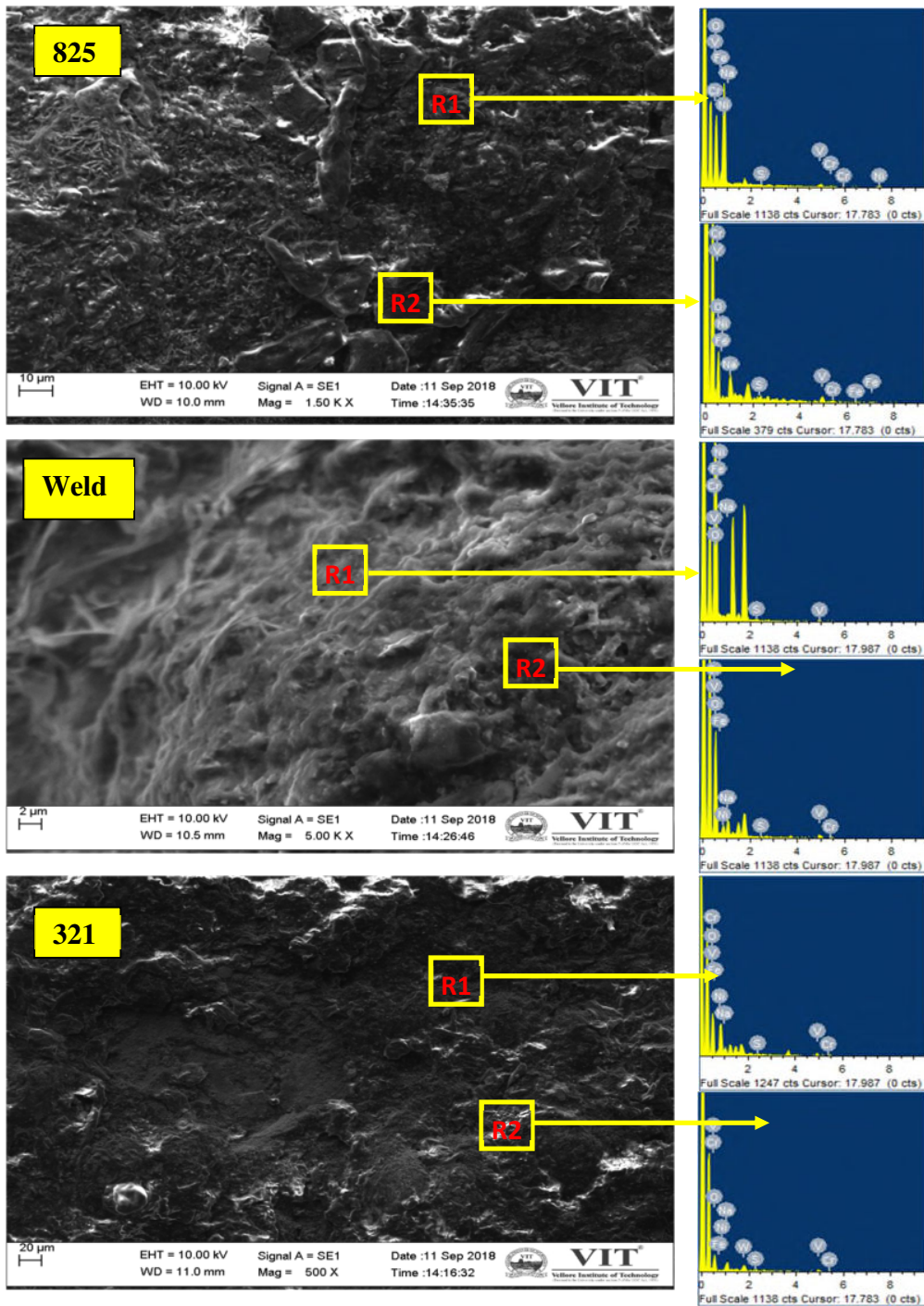


Fig. 11. SEM/EDS analysis of the HVOF-sprayed Ni-20%Cr-coated 825-321 CO<sub>2</sub> laser weldments after hot corrosion in Na<sub>2</sub>SO<sub>4</sub>-60wt%V<sub>2</sub>O<sub>5</sub> environment at 900°C for 50 cycles (R1 and R2 correspond to Region 1 and Region 2, respectively).



Table 5. Elements present in the uncoated 825–321 dissimilar weldments after hot corrosion in Fig. 10

Uncoated weldment	Region	wt%							
		O	Ni	Fe	Cr	Ti	V	S	Na
825	1	32.03	21.15	22.95	18.67	1.27	0.35	1.09	0.65
	2	30.71	22.22	23.67	18.52	0.34	0.64	1.61	2.64
Weld	1	13.46	23.98	33.38	27.84	—	0.63	—	0.71
	2	35.74	16.40	26.48	19.54	0.21	0.29	1.13	0.42
321	1	34.07	17.88	19.71	25.78	1.45	0.46	1.92	0.18
	2	30.68	11.37	25.59	25.90	0.42	0.20	3.27	1.17

Table 6. Elements present in the HVOF-coated 825–321 dissimilar weldments after hot corrosion in Fig. 11

Coated weldment	Region	wt%							
		O	Ni	Fe	Cr	V	S	Na	
825	1	16.57	62.19	3.43	13.18	4.30	0.04	0.30	
	2	10.67	0.63	7.06	55.68	9.73	1.07	5.88	
Weld	1	27.66	32.36	6.94	29.31	1.69	0.23	1.81	
	2	34.67	12.36	8.56	31.60	7.31	0.16	5.34	
321	1	14.60	38.21	4.76	34.90	4.38	0.36	2.82	
	2	22.10	27.24	0.93	35.21	6.25	1.63	6.62	

### 3.9. XRD analysis of scales

The XRD analysis result (Fig. 12) indicates the occurrence of a major phase of  $\text{Fe}_2\text{O}_3$  in the uncoated sample, suggesting that the sample had undergone severe corrosion. Such phase was not prevalent in the case of the HVOF-coated sample; rather, phases such as  $\text{NiO}$ ,  $\text{FeS}$ ,  $\text{TiO}_2$ ,  $\text{NiCr}_2\text{O}_4$ ,  $\text{FeCr}_2\text{O}_4$ , and  $\text{Cr}_2\text{O}_3$  were observed in minor amounts. The XRD result of the Ni–20%Cr-coated weldment shows the presence of the following reaction compounds in the scales:  $\text{NiO}$ ,  $\text{Cr}_2\text{O}_3$ ,  $\text{NiS}$ ,  $\text{CrS}$ ,  $\text{Ni}(\text{VO}_3)_2$ , and spinel oxides such as  $\text{NiCr}_2\text{O}_4$ .

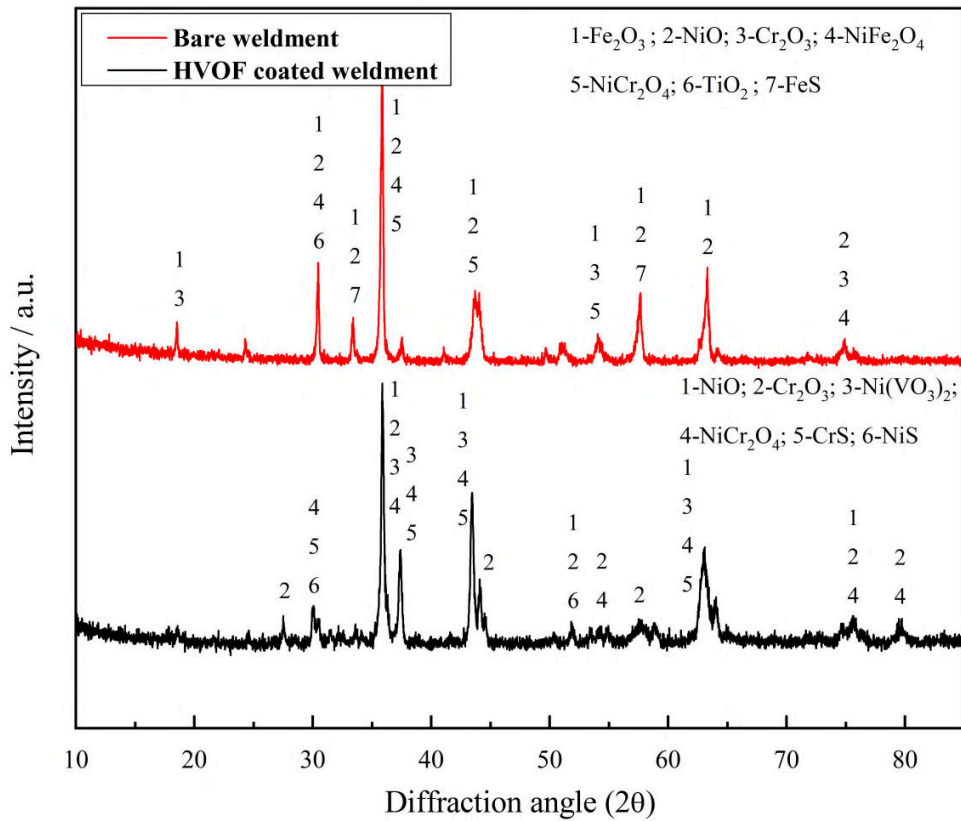


Fig. 12. XRD analysis of the uncoated and HVOF-coated weldments after hot corrosion at 900°C.

### 3.10. EDS line mapping analysis

To analyze the distribution of elements, EDS line mapping analysis was performed on three regions at cross sections: alloy 825, weld, and AISI 321. Fig. 13 shows the result of EDS line mapping cross-sectional analysis of the uncoated dissimilar 825–321 CO<sub>2</sub> laser weldment after hot corrosion at 900°C in an Na<sub>2</sub>SO<sub>4</sub>–60wt%V<sub>2</sub>O<sub>5</sub> environment. From the EDS line mapping analysis result, it can be inferred that the oxygen concentration was higher at the top surface of all the regions, which suggested higher oxidation. Other elements such as Ni and Cr were present in moderate amounts, while Fe was fully present on the regions of alloy 825, weld, and AISI 321; other corrosive elements such as S, V, and Na were also present in the top region. The SEM analysis of the cross section showed the presence of oxide scales on the alloy 825 region in the range of 45–50 μm, and very thin oxide scales were found in the weld and 321 regions due to more oxide scale spallation. High oxide scales spallation could be observed in the region of the AISI 321 region due to the rapid cyclic growth of Fe<sub>2</sub>O<sub>3</sub> oxide scales.

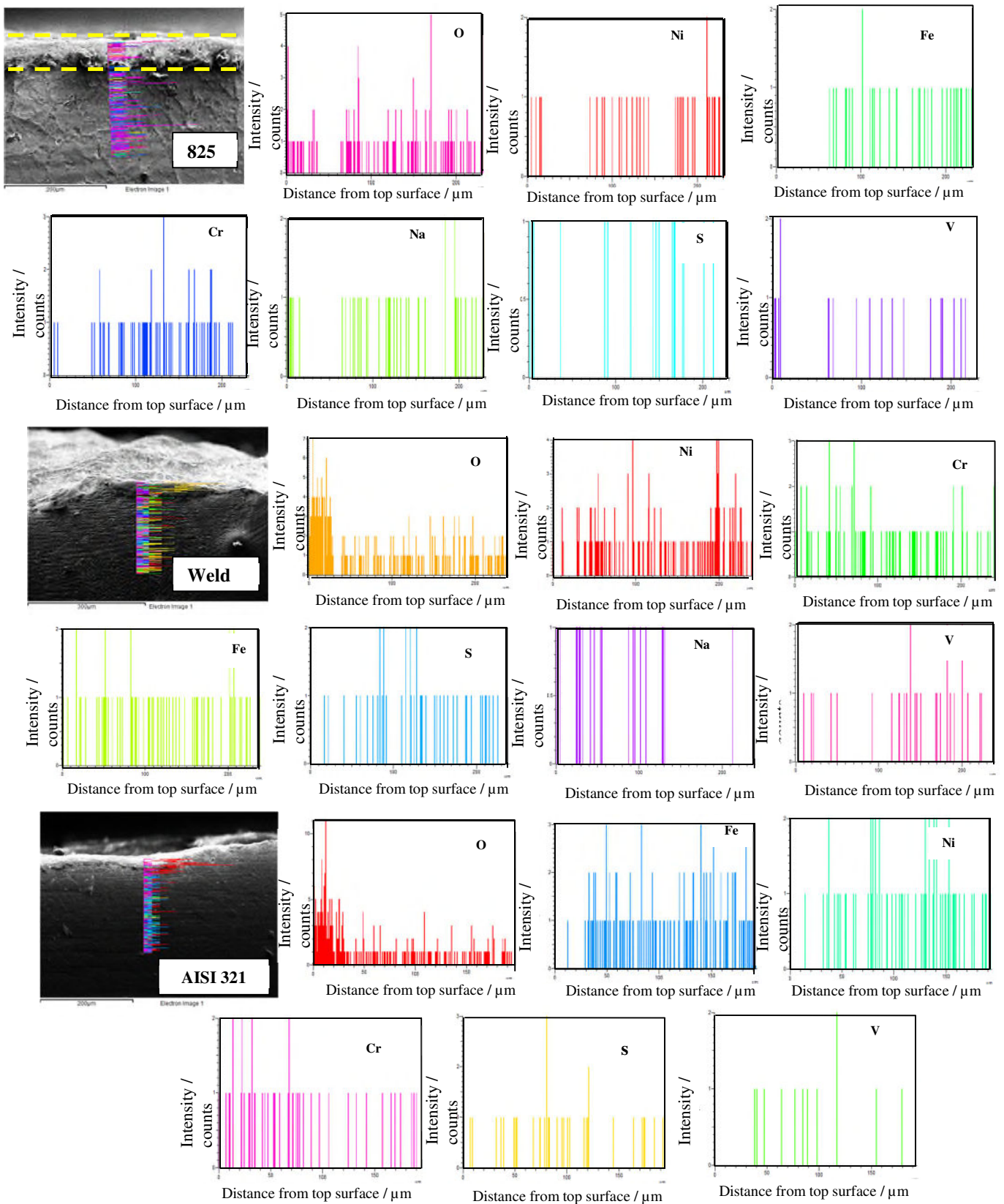


Fig. 13. SEM/EDS line mapping analysis on the uncoated dissimilar 825-321 weldments at cross section after hot corrosion at 900°C in Na<sub>2</sub>SO<sub>4</sub>-60 wt%V<sub>2</sub>O<sub>5</sub> environment.

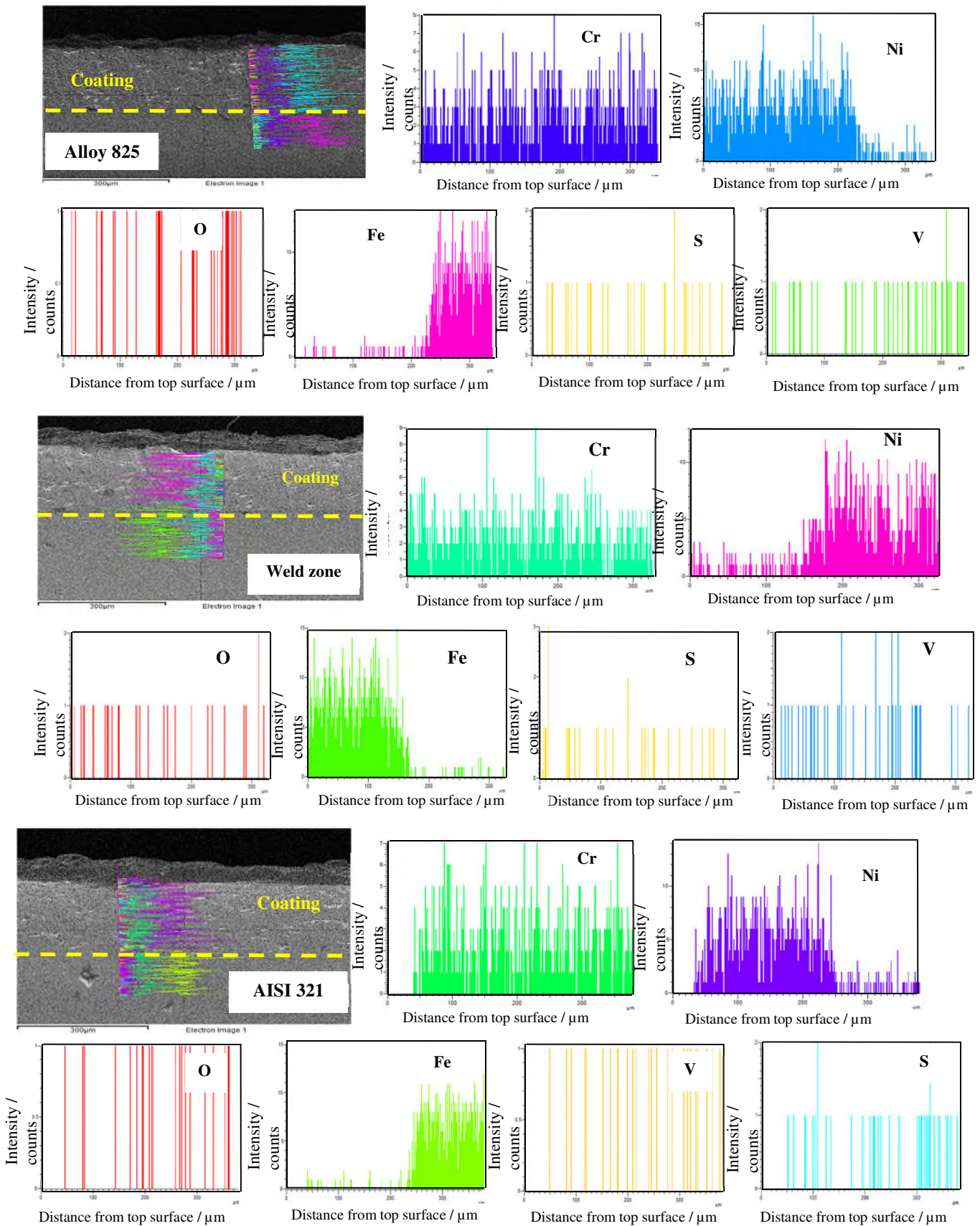


Fig. 14. SEM/EDS line mapping analysis on the HVOF-sprayed dissimilar 825-321 weldments at cross section after hot corrosion at 900°C in  $\text{Na}_2\text{SO}_4$ -60 wt%  $\text{V}_2\text{O}_5$  environment.

The cross-sectional SEM and EDS line mapping analysis results of the HVOF coating performed on the weldment after hot corrosion are depicted in Fig. 14. The SEM analysis result clearly describes that the coating showed good bonding to the weldment, and also no more cracks were found in the coating interface. The results indicate that the top surface of the coating mainly consisted of O, Ni, and Cr, which suggested the formation of NiO and Cr<sub>2</sub>O<sub>3</sub> scales. A minor amount of Fe was found in the coating region near the interface, which indicated the diffusion of Fe from the substrate [19].

### 3.11. Comparison of hot corrosion behaviors of the weldments

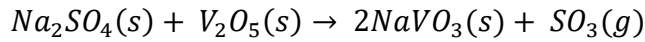
For comparison, a cyclic hot corrosion study was performed on both the uncoated and coated weldments in an aggressive salt atmosphere at 900°C. The uncoated weldment was severely affected by molten salt. The uncoated weldment showed the higher weight gain (8.307 mg·cm<sup>-2</sup>) at the 21<sup>st</sup> cycle, and the parabolic rate constant was  $9.613 \times 10^{-10} \text{ g}^2 \cdot \text{cm}^{-4} \cdot \text{s}^{-1}$ . The weight of the uncoated specimen rapidly increased, which was associated with the continuous oxide scale formation. During the hot corrosion study, the uncoated specimen was severely attacked by corrosion, and more oxide scales spallation could be found due to the development of non-protective Fe<sub>2</sub>O<sub>3</sub> scales. Scales from the uncoated specimen spalled outside the crucible due to spalling and sputtering. Therefore, the weight of the uncoated specimen was reduced after certain cycles. Similar results were observed by Sidhu *et al.* [15] during the hot corrosion study of Inconel 718 in an aggressive Na<sub>2</sub>SO<sub>4</sub>-60wt%V<sub>2</sub>O<sub>5</sub> salt environment at 900°C. The authors reported that the spallation of oxide scales outside the crucible due to sputtering could not be controlled. In the current study, the hot corrosion weight gain/loss data are reported until 50 cycles for both the uncoated and coated specimens. The corrosion rate is calculated only for the maximum weight gain, which corresponds to the 21<sup>st</sup> cycle for the uncoated specimens and the 50<sup>th</sup> cycle for the coated samples.

Iron(III) oxide Fe<sub>2</sub>O<sub>3</sub> is the main scale formed on the uncoated weldment, as confirmed by XRD analysis. The corrosion products could penetrate through the porous Fe<sub>2</sub>O<sub>3</sub> oxide scales and further increase the oxidation rate. More oxide scale spallation occurred during the corrosion experiment due to the variation in the thermal expansion coefficient values between the substrate and the weld region; this also initiates the cracks on the oxide scales, which leads to spallation [16– 17].

The melting points of the salts Na<sub>2</sub>SO<sub>4</sub> and V<sub>2</sub>O<sub>5</sub> are 884 and 690°C, respectively. The melting point of the eutectic mixture of the salts is 610°C, which is much lower than our experiment

temperature (900°C). At 900°C, the salts Na<sub>2</sub>SO<sub>4</sub> and V<sub>2</sub>O<sub>5</sub> combine to form NaVO<sub>3</sub> (Reaction (1), melting point: 610°C), which serves as an oxygen carrier and increases the oxidation rate [17,19]. Consequently, the uncoated weldment gets highly oxidized. Spalling and oxide scale formation were observed to occur simultaneously.

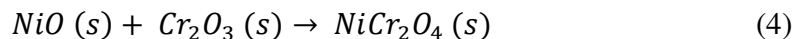
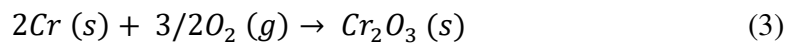
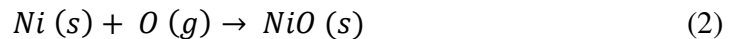
(1)



In the case of the HVOF-coated weldment, gradual weight gain was observed. The coated weldment showed the minimum weight gain and presented a superior corrosion resistance due to the development of Cr<sub>2</sub>O<sub>3</sub>, NiO, and spinel NiCr<sub>2</sub>O<sub>4</sub> protective oxide scales. The protective oxide scales blocked the diffusion of corrosive products. The weight gain and the parabolic rate constant ( $K_p$ ) of the coated weldment were 3.305 mg·cm<sup>-2</sup> and  $0.607 \times 10^{-10}$  g<sup>2</sup>·cm<sup>-4</sup>·s<sup>-1</sup>, respectively. Chatha *et al.* [20] reported that uncoated steel T91 was severely prone to corrosion in the salt environment at 900°C due to non-protective and porous Fe<sub>2</sub>O<sub>3</sub> scale formation; the coated specimen presented superior resistance to corrosion than the uncoated steel, which was associated with the development of protective NiO, Cr<sub>2</sub>O<sub>3</sub>, and spinel NiCr<sub>2</sub>O<sub>4</sub>.

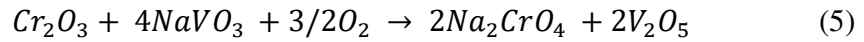
However, some oxide scales spallation occurred in the coated weldment during exposure to salt atmosphere at an elevated temperature. The 321 regions were observed to feature a greater spalling rate compared with the alloy 825 and the weld region. The generation of thermal stress on the oxide scales also initiated crack formation during cyclic heating and cooling. Cracks were present on the corner of the coating due to thermal stress. Molten salts could penetrate into the coating through the pores and cracks on the oxide scales. This could increase the corrosion attack on the coating, which can lead to cracks and oxide scale spallation [21–23].

Protective oxide scales Cr<sub>2</sub>O<sub>3</sub>, NiO, and spinel oxides NiCr<sub>2</sub>O<sub>4</sub> were present in the HVOF-coated weldment, as indicated by the XRD analysis result. The mechanism of oxide scale formation is expressed by the following Reactions (2)–(4):

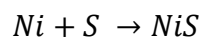


The Cr<sub>2</sub>O<sub>3</sub> scale in the coating acts as a diffusion barrier that prevents the corrosion products from reacting with the substrate material. The Cr<sub>2</sub>O<sub>3</sub> oxide scale also enhances the corrosion resistance and is stable at elevated temperatures because of its high melting point. The protective

oxide scales could be destroyed by the low-melting-point sodium vanadate ( $\text{NaVO}_3$ ), which is explained in Reaction (5). During hot corrosion studies,  $\text{Na}_2\text{SO}_4$  in the environment reacts with the protective oxide scale  $\text{Cr}_2\text{O}_3$  to form  $\text{Na}_2\text{CrO}_4$ , which is volatile. The formed  $\text{Na}_2\text{CrO}_4$  could evaporate as a gas. A similar result has been reported by Mannava *et al.* [24] during the hot corrosion study of Ni-based superalloy 718 in a  $\text{Na}_2\text{SO}_4$ -7.5% $\text{NaVO}_3$ -5% $\text{NaCl}$  environment at 650°C.



The EDS analysis showed the occurrence of a minor amount of Fe in the coated specimen, which suggested the diffusion of Fe from the substrate through cracks and pores in the coating. The NiO oxide scale is partially porous in nature, which may allow the oxidizing and corrosive species reach the coating and substrate, as reported by Chatha *et al.* [20]. In this case, the presence of  $\text{Cr}_2\text{O}_3$  provides sufficient protection to the weldment [19,22]. The spinel oxide  $\text{NiCr}_2\text{O}_4$  is formed by the solid-state reaction between the NiO and  $\text{Cr}_2\text{O}_3$  oxide scale [25]. As the diffusion coefficients of the anions and cations in the formed spinel oxide are smaller than those in the parent oxides, the coated weldment is provided with sufficient corrosion resistance [17,26]. The sulfur from  $\text{Na}_2\text{SO}_4$  can react with alloying elements such as iron, chromium, and nickel to form metal sulfides such as FeS, CrS, and NiS by sulfidation, thereby reducing the environment. Further sulfur could segregate in the oxide scales substrate interface; this might increase the weldments corrosion rate. Reactions (6)–(7) explain the formation of metal sulfides by sulfidation [19,27]. It can be concluded from the present study that the Ni-20wt%Cr-coated weldment showed superior corrosion resistance compared with the uncoated weldment in the given environment.



(7)

#### 4. Conclusions

- (1) Full-penetration dissimilar joints of 825 Ni-based superalloy and AISI 321 stainless steel were successfully obtained by  $\text{CO}_2$  laser welding process.
- (2) Increasing the travel speed of the welding appreciably lowered the welding heat input to a desirable value while keeping the power input constant.
- (3) The tensile test result indicated that fracture occurred in the AISI 321 region, and the fracture mode was confirmed to be ductile by SEM fractography.

- (4) The thermogravimetric experiment results showed that the uncoated specimen presented a high weight gain compared with the HVOF-coated sample.
- (5) The HVOF coating considerably reduced the corrosive effects of the molten salt on the dissimilar laser weldment due to the development of Cr<sub>2</sub>O<sub>3</sub>, NiO, and NiCr<sub>2</sub>O<sub>4</sub> oxide layer.
- (6) From the cross-sectional study, it is inferred that the uncoated weldment featured the occurrence of oxide scale and high corrosion attack, which were not observed in the coated weldment.

### **Acknowledgements**

The authors would like to acknowledge Dr. G. Padmanabham and Mr. Anbu Rasu for facilitating us while conducting the CO<sub>2</sub> laser welding process. The authors thank VIT for providing 'VIT SEED GRANT' for carrying out this research work. The authors would also like to thank Lab in charges of Materials Engineering Technology Laboratory and Advance Materials processing laboratory, VIT-Vellore, India, for providing all the facilities to carry out the research work.

### **References**

1. I.A. Choudhury and M.A. El-Baradie, Machinability of nickel-base super alloys: A general review, *J. Mater. Process. Technol.*, 77(1998), No. 1-3, p. 278.
2. E.O. Ezugwu, J. Bonney, and Y. Yamane, An overview of the machinability of aeroengine alloys, *J. Mater. Process. Technol.*, 134(2003), No. 2, p. 233.
3. A. Thakur, A. Mohanty, and S. Gangopadhyay, Comparative study of surface integrity aspects of Incoloy 825 during machining with uncoated and CVD multilayer coated inserts, *Appl. Surf. Sci.*, 320(2014), p. 829.
4. H. Aytakin and Y. Akçin, Characterization of borided Incoloy 825 alloy, *Mater. Des.*, 50(2013), p. 515.
5. N. Hussain, G. Schanz, S. Leistikow, and K.A. Shahid, High-temperature oxidation and spalling behavior of incoloy 825, *Oxid. Met.*, 32(1989), No. 5, p. 405.
6. K.S. Guan, X.D. Xu, H. Xu, and Z.W. Wang, Effect of aging at 700°C on precipitation and toughness of AISI 321 and AISI 347 austenitic stainless steel welds, *Nucl. Eng. Des.*, 235(2005), No. 23, p. 2485.



7. K.S. Min and S.W. Nam, Correlation between characteristics of grain boundary carbides and creep-fatigue properties in AISI 321 stainless steel, *J. Nucl. Mater.*, 322(2003), No. 2-3, p. 91.
8. M. Schwind, J. Källqvist, J.-O. Nilsson, J. Ågren, and H.-O. Andrén,  $\sigma$ -phase precipitation in stabilized austenitic stainless steels, *Acta Mater.*, 48(2000), No. 10, p. 2473.
9. M. Arivarasu, P. Roshith, R. Padmanaban, S. Thirumalini, K.V. Phani Prabhakar, and G. Padmanabham, Investigations on metallurgical and mechanical properties of CO<sub>2</sub> laser beam welded Alloy 825, *Can. Metall. Q.*, 56(2017), No. 2, p. 232.
10. S. Mohanty, M. Arivarasu, N. Arivazhagan, and K.V. Pani Prabhakar, The residual stress distribution of CO<sub>2</sub> laser beam welded AISI 316 austenitic stainless steel and the effect of vibratory stress relief, *Mater. Sci. Eng. A*, 703(2017), p. 227.
11. S. Kamal, R. Jayaganthan, S. Prakash, and S. Kumar, Hot corrosion behavior of detonation gun sprayed Cr<sub>3</sub>C<sub>2</sub>-NiCr coatings on Ni and Fe-based superalloys in Na<sub>2</sub>SO<sub>4</sub>-60%V<sub>2</sub>O<sub>5</sub> environment at 900°C, *J. Alloys Compd.*, 463(2008), No. 1-2, p. 358.
12. N. Eliaz, G. Shemesh, and R.M. Latanision, Hot corrosion in gas turbine components, *Eng. Fail. Anal.*, 9(2002), No. 1, p. 31.
13. T.S. Sidhu, S. Prakash, and R.D. Agrawal, Studies on the properties of high-velocity oxy-fuel thermal spray coatings for higher temperature applications, *Mater. Sci.*, 41(2005), No. 6, p. 805.
14. T.S. Sidhu, R.D. Agrawal, and S. Prakash, Hot corrosion of some superalloys and role of high-velocity oxy-fuel spray coatings—A review, *Surf. Coat. Technol.*, 198(2005), No. 1-3, p. 441.
15. T.S. Sidhu, S. Prakash, and R.D. Agrawal, Investigations on role of HVOF sprayed Co and Ni based coatings to combat hot corrosion, *Corros. Eng. Sci. Technol.*, 43(2008), No. 4, p. 335.
16. S.M. Muthu, M. Arivarasu, N. Arivazhagan, and M.N. Rao, Investigation of hot corrosion resistance of bare and Ni-20%Cr coated superalloy 825 to Na<sub>2</sub>SO<sub>4</sub>-60%V<sub>2</sub>O<sub>5</sub> environment at 900°C, *Procedia Struct. Integrity*, 14(2019), p. 290.
17. T.S. Sidhu, S. Prakash, and R.D. Agrawal, Hot corrosion studies of HVOF sprayed Cr<sub>3</sub>C<sub>2</sub>-NiCr and Ni-20Cr coatings on nickel-based superalloy at 900°C, *Surf. Coat. Technol.*, 201(2006), No. 3-4, p. 792.

18. H. Singh, T.S. Sidhu, J. Karthikeyan, and S.B.S. Kalsi, Evaluation of characteristics and behavior of cold sprayed Ni–20Cr coating at elevated temperature in waste incinerator plant, *Surf. Coat. Technol.*, 261(2015), p. 375.
19. S.M. Muthu and M. Arivarasu, Investigations of hot corrosion resistance of HVOF coated Fe-based superalloy A-286 in simulated gas turbine environment, *Eng. Fail. Anal.*, 107(2020), art. No. 104224.
20. S.S. Chatha, H.S. Sidhu, and B.S. Sidhu, High temperature hot corrosion behaviour of NiCr and Cr<sub>3</sub>C<sub>2</sub>–NiCr coatings on T91 boiler steel in an aggressive environment at 750°C, *Surf. Coat. Technol.*, 206(2012), No. 19-20, p. 3839.
21. S.M. Muthu and M. Arivarasu, Air oxidation and hot corrosion behavior of bare and CO<sub>2</sub> laser-welded superalloy A-286 at 700°C, *Trans. Indian Inst. Met.*, 72(2019), p. 1607.
22. W.X. Zhou, K.S. Zhou, C.M. Deng, K.L. Zeng, and Y.X. Li, Hot corrosion behavior of HVOF-sprayed Cr<sub>3</sub>C<sub>2</sub>–WC–NiCoCrMo coating, *Ceram. Int.*, 43(2017), No. 12, p. 9390.
23. M.Z. Li, Y.X. Cheng, L. Guo, C.L. Zhang, Y.C. Zhang, S.X. He, and F.X. Ye, Preparation of plasma sprayed nanostructured GdPO<sub>4</sub> thermal barrier coating and its hot corrosion behavior in molten salts, *Ceram. Int.*, 43(2017), No. 10, p. 7797.
24. V. Mannava, A.S. Rao, N. Paulose, M. Kamaraj, and R.S. Kottada, Hot corrosion studies on Ni-base superalloy at 650°C under marine-like environment conditions using three salt mixture (Na<sub>2</sub>SO<sub>4</sub> + NaCl + NaVO<sub>3</sub>), *Corros. Sci.*, 105(2016), p. 109.
25. S. Kamal, R. Jayaganthan, and S. Prakash, Evaluation of cyclic hot corrosion behaviour of detonation gun sprayed Cr<sub>3</sub>C<sub>2</sub>–25%NiCr coatings on nickel- and iron-based superalloys, *Surf. Coat. Technol.*, 203(2009), No. 8, p. 1004.
26. T.S. Sidhu, S. Prakash, and R.D. Agrawal, A comparative study of hot corrosion resistance of HVOF sprayed NiCrBSi and Stellite-6 coated Ni-based superalloy at 900°C, *Mater. Sci. Eng. A*, 445-446(2007), p. 210.
27. M. Arivarasu, M. Venkatesh Kannan, K. Devendranath Ramkumar, and N. Arivazhagan, Hot-corrosion resistance of dissimilar AISI 4340 and AISI 304L weldments in the molten salt environment at 600°C, *Corros. Eng. Sci. Technol.*, 52(2017), No. 2, p. 114.